

# REPORT DOCUMENTATION PAGE

AFRL-SR-AR-TR-03-

0311

The public reporting burden for this collection of information is estimated to average 1 hour per response, including gathering and maintaining the data needed, and completing and reviewing the collection of information. Send comments, including suggestions for reducing the burden, to Department of Defense, Washington Headquarters Service, 1215 Jefferson Davis Highway, Suite 1204, Arlington, VA 22202-4302. Respondents should be aware that notwithstanding any other notation that may appear hereon, it does not display a currently valid OMB control number. PLEASE DO NOT RETURN YOUR FORM TO THE ABOVE ADDRESS.

1. REPORT DATE (DD-MM-YYYY) 29-07-2003		2. REPORT TYPE Final Report		3. DATES COVERED (From - To) March 1999 - August 2002	
4. TITLE AND SUBTITLE Development of Electrochemical Capacitor Technology for DOD Applications				5a. CONTRACT NUMBER F49620-99-1-0183	
				5b. GRANT NUMBER F49620-99-1-0183	
				5c. PROGRAM ELEMENT NUMBER NA	
				5d. PROJECT NUMBER NA	
6. AUTHOR(S) Dr. Allen Apblett				5e. TASK NUMBER NA	
				5f. WORK UNIT NUMBER NA	
7. PERFORMING ORGANIZATION NAME(S) AND ADDRESS(ES) Oklahoma State University College of Arts & Sciences 210 Life Science East Stillwater, OK 74078-3015				8. PERFORMING ORGANIZATION REPORT NUMBER CAGE Code OU784	
9. SPONSORING/MONITORING AGENCY NAME(S) AND ADDRESS(ES) AFOSR/NL 4015 Wilson Blvd., Room 713 Arlington, VA 22203-1954				10. SPONSOR/MONITOR'S ACRONYM(S) OSU	
				11. SPONSOR/MONITOR'S REPORT NUMBER(S)	
12. DISTRIBUTION/AVAILABILITY STATEMENT Approve for Public Release: Distribution Unlimited					
13. SUPPLEMENTARY NOTES					
14. ABSTRACT See enclosed abstract					
15. SUBJECT TERMS					
16. SECURITY CLASSIFICATION OF:			17. LIMITATION OF ABSTRACT	18. NUMBER OF PAGES	19a. NAME OF RESPONSIBLE PERSON Dr. Allen W. Apblett
a. REPORT	b. ABSTRACT	c. THIS PAGE			19b. TELEPHONE NUMBER (include area code) 405-744-5943

20030818 003

**FINAL REPORT**  
**March 1999-August 2002**

**AIR FORCE OFFICE OF SCIENTIFIC RESEARCH**

**PROJECT TITLE:**

**Development of Electrochemical Capacitor Technology for DOD Applications**

**PRINCIPLE INVESTIGATOR:**

**Allen W. Apblett**  
**Department of Chemistry**  
**Oklahoma State University**  
**Stillwater, OK 74078-3071**  
**Phone: 405-744-5943**  
**Fax: 405-744-6007**  
**E-mail: [apblett@okstate.edu](mailto:apblett@okstate.edu)**

**Agreement # F49620-99-1-0183**

## OBJECTIVES

The major objective of this project was to make a positive impact on the development of supercapacitors that are vital to the production of electrical vehicles and low-maintenance power sources for military applications. The research takes advantage of novel ceramic precursors to elaborate new, economical synthetic methods for the preparation of electrode materials that are currently under investigation for use in electrochemical capacitors. It is anticipated that these precursors will allow the preparation of the desired materials via environmentally-friendly water-based processes that don't produce corrosive by-products. The research also targeted the identification of new, superior electrode materials based on an approach using water-based bimetallic or multimetallic precursors. The ceramic precursors developed in this investigation are also expected to impact other applications besides supercapacitors and any opportunity to make this research responsive to the materials needs (especially electrodes) of the military will be pursued.

## ACCOMPLISHMENTS

### Metallo-Organic Precursors for Ruthenia

The research project targeted improved synthetic methods for nanocrystalline or amorphous ruthenium dioxide, a promising material for electrochemical supercapacitors. Ruthenium dioxide is a d-band metallic conductor with a conductivity of  $10^4$  S/cm [1] and also displays useful catalytic properties leading to its utility in a variety of applications.  $\text{RuO}_2$  displays extremely low overpotential for chlorine and oxygen evolution by electrochemical means and is thus used extensively as an electrocatalyst [2, 3]. In combination with  $\text{TiO}_2$ ,  $\text{RuO}_2$  forms dimensionally-stable electrodes that are the mainstay of the chlor-alkali process in which brine is electrolyzed to produce the commodities  $\text{NaOH}$  and  $\text{Cl}_2$ . Ruthenium oxide can also serve as a cathode material for hydrogen evolution and can serve as a replacement for noble metal catalysts with much improved resistance to poisoning. It is also useful for photochemical processes such as water decomposition and as an electrode material for supercapacitors (also known as electrochemical capacitors). In the latter application, the high capacitance of  $\text{RuO}_2$  ( $150\text{--}260 \mu\text{F}/\text{cm}^2$ ) is an order of magnitude higher than carbon electrodes that have typically been used for this purpose [4]. Ruthenium also forms a series of amorphous hydrous oxides of varying water (or hydroxide) content and with ruthenium in a variety of mixed oxidation states. These materials can transport and store both protons and electrons, a property that is exploited in both supercapacitors and fuel cells. In the latter application, hydrous ruthenia has been demonstrated to be important to the operation of Pt-Ru direct methanol fuel cell catalysts [5]. In the case of supercapacitors,  $\text{RuO}_x\text{H}_y$  acts as a "proton condenser" that bears surface sites that can be reversibly reduced and oxidized with simultaneous exchange of protons with the contacting electrolyte (Equation 1). These electrochemical reactions result in a high specific capacitance of  $1200 \mu\text{F}/\text{cm}^2$  and nearly featureless voltammograms, making hydrous ruthenia an excellent electrode material for supercapacitors [6-8].

There is a need to find improved methods for preparing electrode materials with high surface area and controlled porosity. A variety of methods have been used for this purpose. For example,  $\text{RuO}_2$  electrodes have been prepared by thermal pyrolysis of  $\text{RuCl}_3$  on metal substrates [5], by a sol-gel process involving hydrolysis of  $\text{RuCl}_3$  by  $\text{NaOH}$  [6], and by electrochemical

surface oxidation of ruthenium metal [9]. The metallo-organic deposition (MOD) method [10, 11] provides an interesting alternative for the preparation of the ruthenium oxide films required for electrochemical capacitors. MOD avoids the generation of toxic or corrosive gases during the deposition process, is very inexpensive, and allows the possibility of control of porosity in the final material. MOD is a non-vacuum, solution-based method of depositing thin films. In the MOD process, a suitable metallo-organic precursor dissolved in an appropriate solvent is coated on a substrate by spin-coating, screen printing, or spray- or dip-coating. The soft metallo-organic film is then pyrolyzed in air, oxygen, nitrogen or other suitable atmosphere to convert the precursors to their constituent elements, oxides, or other compounds. Shrinkage generally occurs only in the vertical dimension so conformal coverage of a substrate may be realized. Metal carboxylates with long slightly-branched alkyl chains (e.g. 2-ethylhexanoate or neodecanoate) are often used as precursors for ceramic oxides since they are usually air-stable, soluble in organic solvents, and decompose readily to the metal oxides. The choice of precursors in this study was the trinuclear ruthenium oxocarboxylate clusters,  $\text{Ru}_3\text{O}(\text{O}_2\text{CR})_7 \cdot 3\text{H}_2\text{O}$ . These compounds have the advantage that they are readily prepared, are air- and water-stable, and are soluble in organic solvents. The latter property allows the precursors to be readily processed into thin films by spin- or dip-coating, painting, screen-printing, etc. The R-group on the carboxylate is easily varied, so the chemical and physical properties of the precursors are readily tuned.

Ruthenium acetate is commercially-available but is somewhat expensive but it can conveniently be prepared using a modification of the original synthesis by Wilkinson and co-workers [12]. The preparation involves reaction of hydrated ruthenium chloride with sodium acetate in a hot ethanol/acetic acid medium. The main difficulty with this reaction is separation of the product from the sodium chloride by-product. In this investigation it has been found that extraction of the ruthenium acetate into 1:2 propanol:hexane to be an effective means of separation. The other metal carboxylates were prepared in a similar manner with omission of excess acid in the solvent system. Most of the derivatives with larger alkyl groups or phenyl residues could be dissolved in pentane and were readily separated from sodium chloride.

The thermal gravimetric analysis (TGA) of the precursors demonstrated that they first dehydrated and then decomposed to ruthenium oxide in two overlapping steps. The TGA trace of the trimethylacetate derivative is shown in Figure 1 and is representative of most of the carboxylates. The decomposition of the carboxylates tends to start slowly but when sufficient  $\text{RuO}_2$  has been generated it becomes rapid and highly exothermic since the ruthenium acts as a combustion catalyst. For example, an experiment using 5 mg of ruthenium trimethylacetate resulted in an almost instantaneous jump in temperature of the sample, the aluminum pan, and the sample holder from 185°C to 297°C. The combustion process involves cycling between Ru(IV) and reduced forms of ruthenium, so that, in the absence of an adequate supply of oxygen, a mixture of ruthenium oxidation states is produced. In fact, the composition of the product could be varied by changing the amount of sample used or the flow rate of air. With very small amounts of precursor, ignition does not occur and a smooth decomposition proceeds to give a hydrous ruthenium oxide. In all cases where ruthenium metal had formed, reoxidation to give ruthenium(IV) oxide occurred slowly, starting at 500°C and finishing at approximately 900°C.

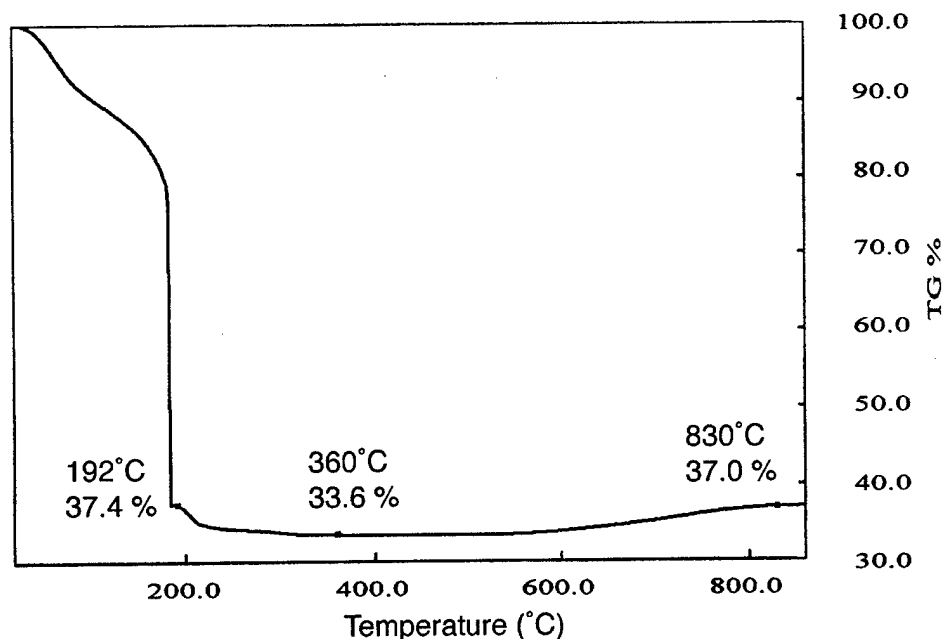


Figure 1. TGA Trace for Ruthenium Trimethylacetate

X-ray powder diffraction of bulk samples prepared in a muffle furnace at 200°C demonstrated that the product isolated immediately after the combustion process was amorphous. Upon sintering 250°C, the product from ruthenium acetate displayed broad reflections in its XRD pattern (Figure 2) corresponding to nanocrystalline ruthenium metal (average size 1.4 nm) while at 350°C, a mixture of ruthenium (IV) oxide and ruthenium metal was detected. The XRD pattern of the ceramic produced by sintering of the ruthenium trimethylacetate product at 360°C (Figure 3) also contained reflections corresponding to both ruthenium (IV) oxide and ruthenium metal, each with a fairly small average crystallite size (2.3 nm and 2.7 nm, respectively). Upon heating to sufficiently high temperature both ceramic products produced highly crystalline RuO<sub>2</sub>. Oxidation of the ruthenium metal is detectable by a weight gain in the TGA experiment and starts at approximately 500°C and is complete at 900°C.

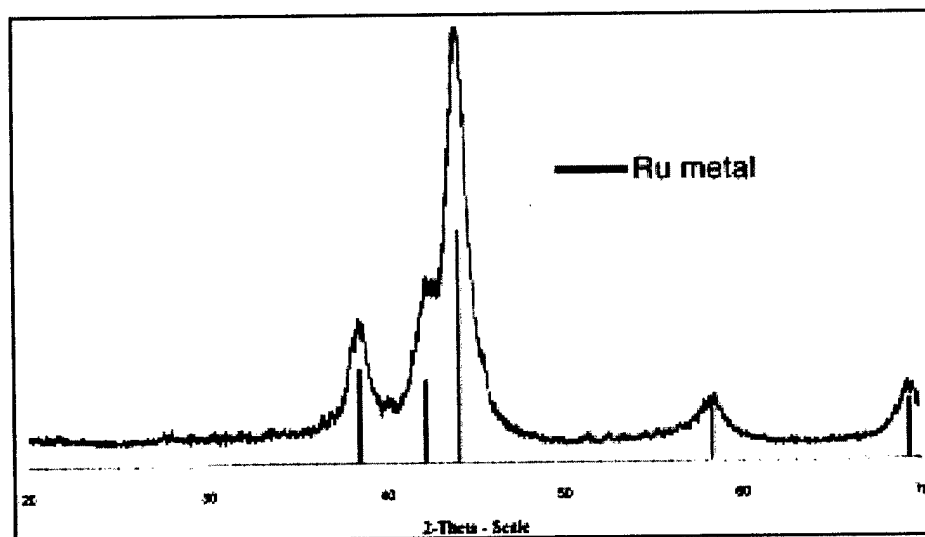


Figure 2. XRD Pattern of Ceramic from Ruthenium Acetate at 250°C

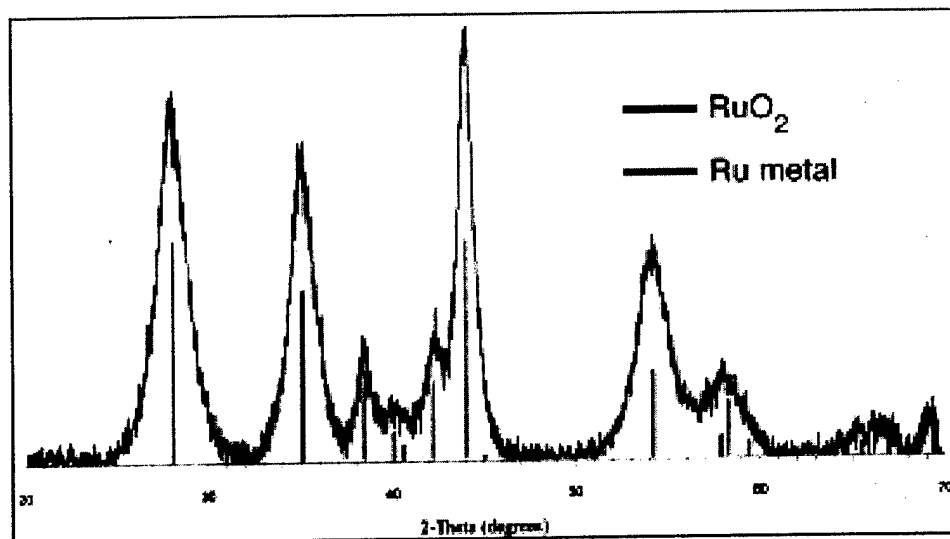


Figure 3. XRD Pattern of Ceramic from Ruthenium Trimethylacetate at 360°C

The temperature at which each individual precursor reached the point where the organics had been removed varied from 200°C to 350°C. More importantly, the surface area of the ceramic product showed a profound dependence on the nature of the carboxylate (Table 1). This is in accordance with our expectation that the porosity could be controlled by the amount of organic that burned out of the precursor as shown in Figure 4. Interestingly, it was found that simply increasing the chain length of the carboxylate did not have a major effect on the surface area but adding methyl or phenyl groups to the chain had profound effects. The results suggest that the surface area could be improved further using even bulkier carboxylates.

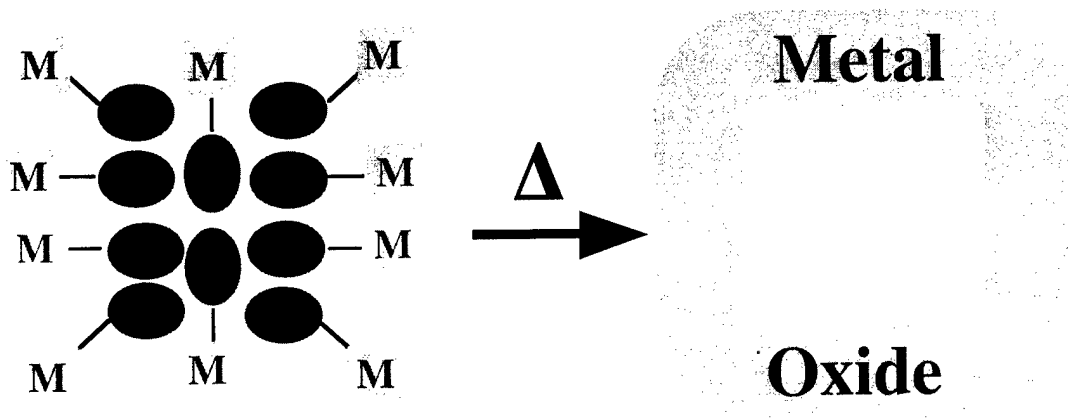


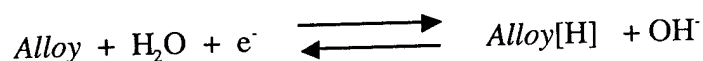
Figure 4. Production of Porosity by Burn-Out of Organic Fragments from Metal Carboxylates

TABLE 1. Surface Areas of Ruthenium Oxide from Ruthenium carboxylates

Compound	Temperature (°C)	Surface Area (m <sup>2</sup> /g)
Ruthenium Acetate	250	10.5
Ruthenium Laurate	215	6.6
Ruthenium Stearate	350	41.8
Ruthenium Trimethylacetate	200	51.8
Ruthenium Phenylacetate	350	74.0
Ruthenium Diphenylacetate	225	90.5
Ruthenium Triphenylacetate	225	105.1

### Solution Growth of Nickel Hydroxide

Nickel hydroxide has been extensively applied as active material for positive electrode of secondary alkaline batteries because of its remarkable cycling reversibility. During the oxidation process,  $\beta$  and  $\alpha$ -Ni(OH)<sub>2</sub> are respectively converted to the  $\beta$  and  $\gamma$  NiOOH phases. On prolonged charging  $\beta$ -Ni(OH)<sub>2</sub> is converted to  $\gamma$ -NiOOH causing irreversible damage to the electrode due to the accompanying mechanical deformation. On the contrary,  $\alpha$ -Ni(OH)<sub>2</sub> is reversibly cycled to  $\gamma$ -NiOOH without any mechanical alteration. Due to the alpha phase instability in alkaline environment,  $\beta$ -Ni(OH)<sub>2</sub> is frequently preferred for precursor material in alkaline batteries. The first nickel-based rechargeable cell, invented by Thomas Edison in 1890, consisted of a nickel hydroxide cathode coupled with an iron anode and an alkaline electrolyte using potassium hydroxide (Ni / 2NiOOH / Fe). Despite a very long cycle life and robustness, the Ni/Fe alkaline cell suffers from deficiencies stemming from the iron electrode, which tends to undergo self-discharge on standing as a result of corrosion. The invention of this rechargeable nickel battery paved the way for the development of other types of nickel-based cells, the common nickel cadmium cell (Ni-Cd), the Ni-Zn cell, the Ni-hydrogen battery (aerospace batteries), and nickel metal hydride cells used for the powering of portable electronic devices such as the lap-top computers, wireless telephones and more recently electric vehicles. The Ni-Cd alkaline battery is the most widely manufactured despite a modest specific energy (30-40 Wh/kg). It is commonly used in replacement for lead/acid batteries in the automotive industry (ignition, starting, and lighting) and in certain airplanes. Ni-MH rechargeable cells incorporate a different type of anode that allows hydrogen storage in a specialized metal structure, an alloy of composition AB<sub>5</sub> (example: LaNi<sub>5</sub>) or AB<sub>2</sub>. Upon discharge, hydrogen is inserted within the alloy lattice without bonding to it, and is released during the charging process (see Equation 3 below). One drawback to the Ni-MH cell is rapid self-discharge, reliable means for hydrogen storage still needs to be found.



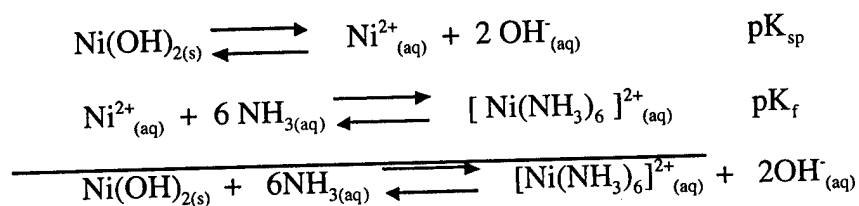
Ni-MH rechargeable battery: Anode reaction

In general, nickel-based batteries are excellent for applications that require rechargeable batteries that take very little time to recharge, and will survive under less than optimal conditions.

In this investigation, solution growth methods were developed for nickel hydroxide as a promising electrode material. Not only might such electrodes be useful for batteries but if made sufficiently electrically-conductive they could be fashioned into alkaline supercapacitors. Solution growth also known as chemical bath deposition is a promising alternative to metallorganic deposition for the preparation of metal oxide coatings. The typical solution growth process cannot be used for deposition of divalent third-row transition metal oxides for several reasons. In the usual process the anion required for the desired material (e.g. sulfide) is generated slowly in the form of a strongly chelated metal so that the constituent cations and anions are assembled into a thin film by an ion-by-ion deposition process. Since oxide ions are protonated by water, the direct solution growth metal oxide films from aqueous is precluded for most metals. However, hydroxides can be prepared by solution growth by using the hydrolysis of urea to slowly raise solution pH. Unfortunately, for the metals of interest in this study, nickel and zinc, this metal would lead to deposition of carbonate rather than the hydroxides. Therefore, in this investigation, a new method was developed for solution growth of nickel hydroxide. This new process takes advantage of the strong complexation of nickel by ammonia ( $K_f [\text{Ni}(\text{NH}_3)_6]^{2+} = 5.5 \times 10^8$ ) to overcome the insolubility of  $\text{Ni}(\text{OH})_2$  in water ( $K_{sp} = 2.0 \times 10^{-15}$ ). Once a solution is saturated with  $\text{Ni}(\text{OH})_2$  it is susceptible to deposition of this metal hydroxide as the ammonia evaporates from the solution.

Addition of nickel hydroxide to concentrated ammonia leads to formation of a dark blue color attributable to  $[\text{Ni}(\text{NH}_3)_6]^{2+}$ . The concentration of nickel hexammine was determined by measuring the weight of  $\text{Ni}(\text{OH})_2$  deposited after complete evaporation of the solvent, and drying of the solid under vacuum. The average  $[\text{Ni}^{2+}]_{av}$  was found to be  $0.139 \pm .006$  mol/L

The chemical equation representing the overall equilibrium is the sum of the  $\text{Ni}(\text{OH})_2$  dissolution reaction and the Ni(II) complexation reaction with ammonia.



$$P_s = -\log \left( \frac{[\text{Ni}(\text{NH}_3)_6]^{2+} [\text{OH}^-]_{tot}}{[\text{NH}_3]^6} \right)$$

Where  $[\text{Ni}(\text{NH}_3)_6]^{2+}$ ,  $[\text{NH}_3]$  and  $[\text{OH}^-]$  are concentrations in mol/L



Ps is computed by using the average  $[\text{Ni}(\text{NH}_3)_6]^{2+}$  concentration determined above (0.139 M).  $[\text{OH}]_{\text{tot}}$  in the ammonia solution after saturation with  $\text{Ni}(\text{OH})_2$ , is determined by measuring the pH (13.7).  $[\text{NH}_3]$  is the concentration after complexation of  $\text{Ni}^{2+}$  with 6 ammonia equivalents, where  $[\text{NH}_3]_{\text{initial}}$  is the concentration of the initial ammonium hydroxide solution<sup>46</sup>.  $[\text{NH}_3]_{\text{equilibrium}}$  was calculated by subtracting the concentration of  $[\text{NH}_4^+]$  formed at equilibrium from the remaining as follows:

$$\begin{aligned} [\text{NH}_3]_{\text{equilibrium}} &= [\text{NH}_3] - [\text{NH}_4^+]_{\text{equilibrium}} \\ [\text{NH}_3]_{\text{equilibrium}} &= ([\text{NH}_3]_{\text{initial}} - 6[\text{Ni}^{2+}]) - ([\text{OH}]_{\text{tot}} - 2[\text{Ni}^{2+}]) \\ &= 14.53 - 6 \times 0.139 - 10^{-0.3} + 2 \times 0.139 \\ &= 13.47 \text{ M} \end{aligned}$$

By using Equation 8, Ps can be easily calculated and is found to be 8.23

The pKs determined experimentally is significantly higher than the theoretical value of 6.0 calculated as the sum of the  $\text{pK}_f$  and  $\text{pK}_{\text{sp}}$ . In other words, the solubility of nickel hydroxide in conc. ammonia is about two orders lower than predicted. The theoretical value does assume ideal behavior (i.e. low concentrations where activity is proportional to concentration) and zero ionic strength. Since the experimental conditions deviate significantly from these assumptions, this could account for a discrepancy in the values of pKs. As well, assumptions made concerning the speciation of  $\text{Ni}(\text{OH})_2$  in the aqueous ammonia solution could be enormous- for example, formation of  $[\text{Ni}(\text{OH})(\text{NH}_3)_5]^+$  complex could lead to significant perturbation of the experimental result. Also the concentration of water in concentrated ammonia is reduced to 40 M from 56 M for pure water this too, could have a major effect on solubility. Evaporation of ammonia during the dissolution of  $\text{Ni}(\text{OH})_2$  may also play a minor role in the depressing the final nickel concentration. The results do also show, however, that simple use of formation constant and solubility products do not make an adequate prediction of the solubility of the metal hydroxides in concentrated ammonia.

The solution growth of  $\text{Ni}(\text{OH})_2$  depends on the slow formation of hexa-aqua nickel (II) conc. as the ammonia evaporates form solution. Either this ion, or an intermediate ammonia complex  $[\text{Ni}(\text{H}_2\text{O})_x(\text{NH}_3)_{(6-x)}]^{2+}$ , interacts with hydroxide ion to form a hydroxide complex, probably occurs by deprotonation of the coordinated aqua ligand. The addition of a second hydroxide ion or deprotonation of a second aqua ligand could generate a  $\text{Ni}(\text{OH})_2$  complex that would be prone to precipitation. For solution growth of nickel hydroxide films to occur, it is desirable that the second reaction occur on the surface of the substrate or that the putative  $\text{Ni}(\text{OH})_2$  complex diffuse and deposit precipitating from the bulk solution.

The rate of deposition of  $\text{Ni}(\text{OH})_2$  was determined by placing 30 ml of  $\text{Ni}(\text{OH})_2$ -saturated ammonia in eight identical beakers. The amount of nickel hydroxide deposited after various time intervals was determined by emptying the remaining solution from the beaker, placing under vacuum overnight, and weighing. After 120 hours, the solution was colorless indicating that all the nickel(II) initially dissolved had precipitated. The plot of  $\text{Ni}(\text{OH})_2$  film weight versus time is shown in Figure 5. The deposition occurs progressively at a almost constant rate up to 90 hours, then slows down and stops after 120mn. The deposition does occur as a solution growth process and yields homogeneous pale green films on the sides of the beaker.

The morphology of Nickel hydroxide prepared from the ammonia solution is quite unusual, as illustrated on the scanning electron micrograph shown in Figure 6. Large spheres with a diameter of 3.8  $\mu\text{m}$  appear to consist of extremely small needles of  $\text{Ni}(\text{OH})_2$ . Despite the very porous looking microstructure and a rather small particle size the surface area measurement

listed in Table 2 is surprisingly small possibly due to the adsorbed and intercalated water molecules.

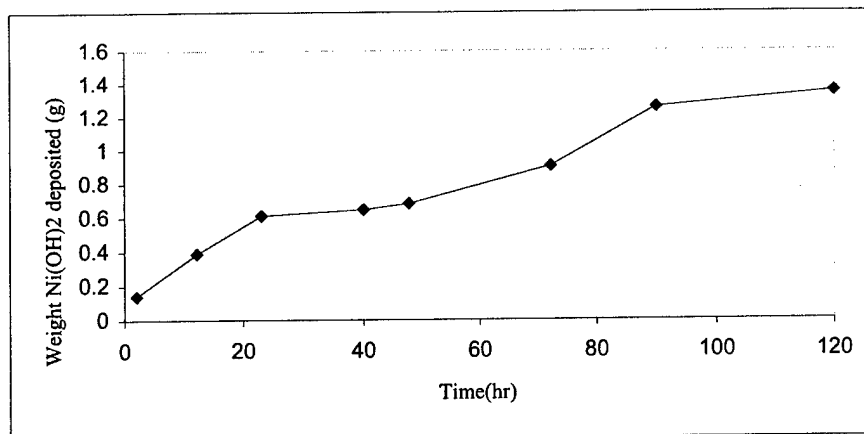


Figure 5. Nickel Hydroxide Deposition Rate

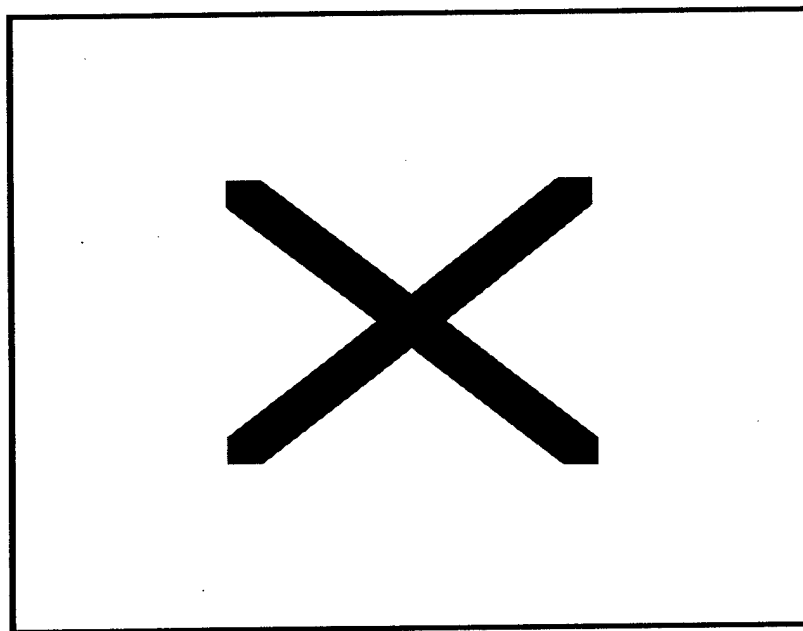


Figure 6. SEM of  $\beta$ -Ni(OH)<sub>2</sub> from Solution Growth

A typical X-ray diffraction pattern for nickel hydroxide synthesized by the ammonia solution growth is shown in Fig. 7 (a) with a common Ni(OH)<sub>2</sub> pattern obtained from precipitation Fig. 7 (b) as a basis for comparison. The considerably higher intensity of certain reflections of the ammonia grown hydroxide is an indication of a larger crystallite size in specific crystallographic directions including [001], [101], and [102]. The increase in crystallite size is also accompanied by a decrease of the NiO inter-planar distance from 4.59 Å to 4.72 Å, as evidenced by a shift towards smaller  $d$  of the 001 plane reflection peak. As a result of the  $d_{001}$  change, the  $d$ -spacings of the peaks including (101) and (102) are also slightly displaced but to a lesser extent. This suggests the slow precipitation of Ni(OH)<sub>2</sub> from aqueous ammonia yields a highly ordered layered compound, in contrast with the poorly crystallized Ni(OH)<sub>2</sub> from the rapid precipitation

of a nickel nitrate solution. Previous work on the preparation of nickel hydroxide from hydrothermal treatment reported an identical X-ray  $\text{Ni(OH)}_2$  pattern and microstructural characteristics. This two-step method consisted of hydrothermally treating at  $200^\circ\text{C}$  an aqueous suspension of turbostratic  $\alpha\text{-Ni(OH)}_2$  previously prepared by the precipitation by treatment of a nickel nitrate solution with base.

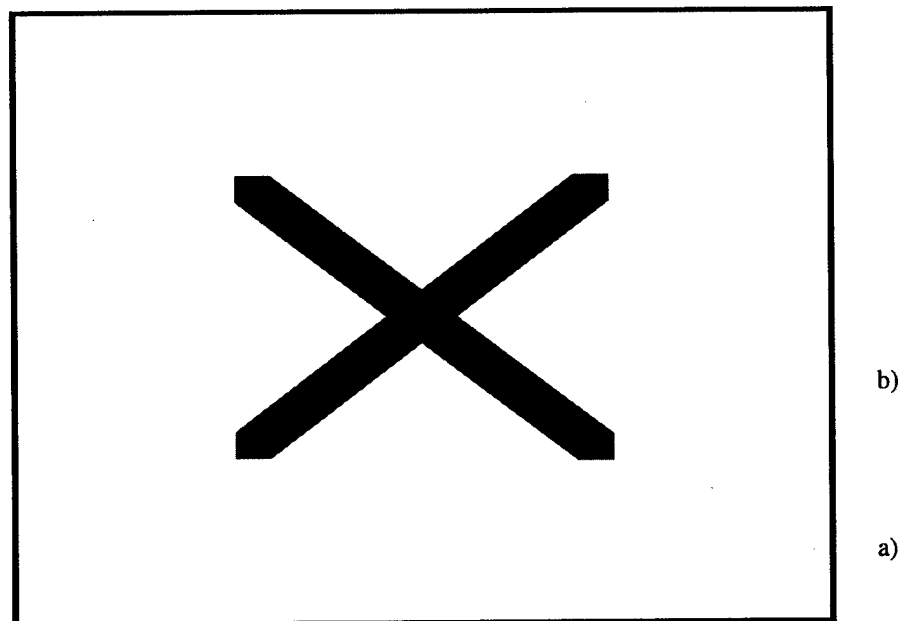


Figure 7. XRD of  $\beta\text{-Ni(OH)}_2$  from Solution Growth Method (b), and from Precipitation Method from a  $\text{Ni(NO}_3)_2$  solution with Strong Base(a)

Infrared spectroscopy is a good indicator of short-range structure and very useful for characterizing  $\text{Ni(OH)}_2$  phases. The formation of the  $\beta$  form of  $\text{Ni(OH)}_2$  demonstrated by using X-ray diffraction was confirmed in the infrared spectrum showed in Figure 8. The existence of an intense sharp absorption at  $3642\text{cm}^{-1}$  is characteristic of O-H stretching vibration,  $\nu_{\text{OH}}$ , of non hydrogen-bonded OH groups. The broad shoulder at  $3400\text{cm}^{-1}$  is attributed to the  $\nu_{\text{OH}}$  of hydrogen-bonded OH groups of adsorbed water molecules. A weak irregular band from  $1500$  to  $1696\text{ cm}^{-1}$  includes the water angular deformation at  $1653\text{ cm}^{-1}$  and adsorbed ammonia molecules deformation vibration.

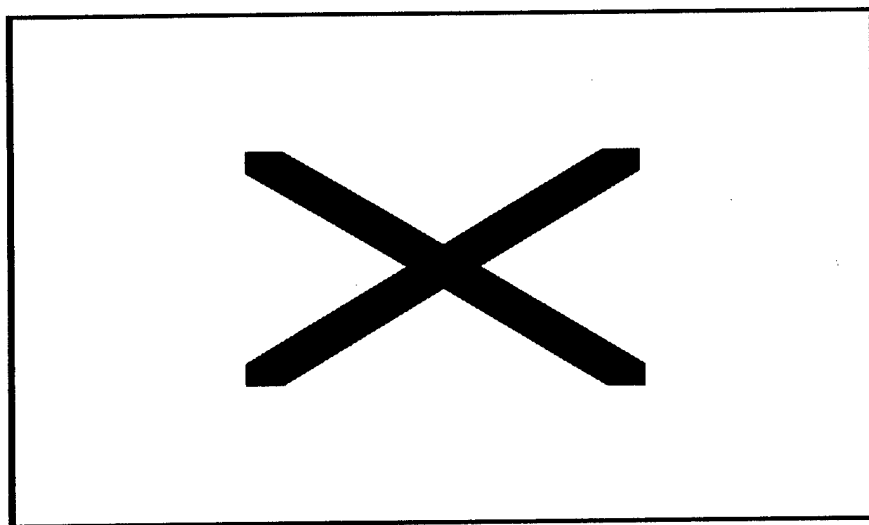


Figure 8. Infrared Spectrum of  $\beta$ -Ni(OH)<sub>2</sub> from Solution Growth Method

The thermal decomposition pattern shown in Figure 9 is very similar to those published in early studies. Gradual elimination of adsorbed molecules such as water constitutes the first weight loss. The slightly endothermic process stops at 180°C. The dehydrated sample then undergoes dehydration to yield NiO at 500°C with release of heat. The decomposition of Ni(OH)<sub>2</sub> grown from the sulfate or nitrate salt solutions usually extends over a wider temperature range necessary to pyrolyze the adsorbed anions such as SO<sub>4</sub><sup>2-</sup>, CO<sub>3</sub><sup>2-</sup> and NO<sub>3</sub><sup>-</sup> present in the mother solution.

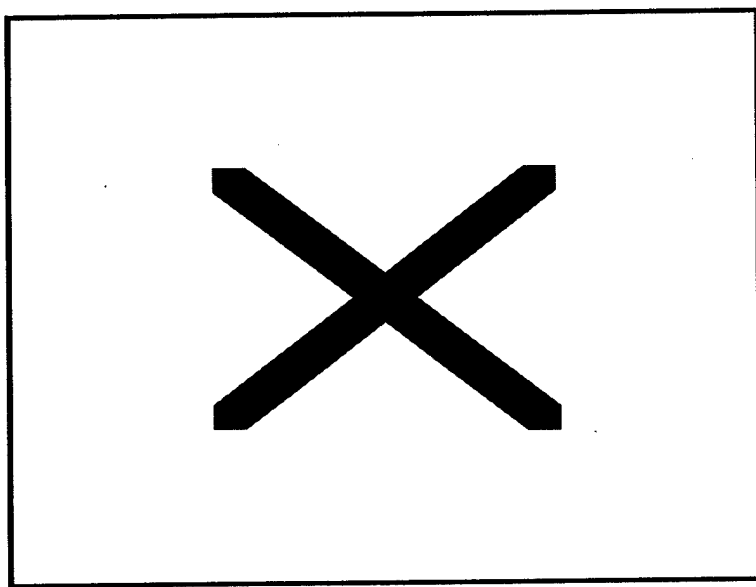


Figure 9. TGA of  $\beta$ -Ni(OH)<sub>2</sub> from Solution Growth Method

Table 2. Surface Area of  $\beta$  and  $\alpha$ -Ni(OH)<sub>2</sub> from Solution Growth Method

Compound	Surface area (m <sup>2</sup> /g)
$\beta$ -Ni(OH) <sub>2</sub> from solution growth	20.6
$\alpha$ Ni <sub>0.87</sub> Al <sub>0.13</sub> (OH) <sub>2.13</sub>	37.1
$\alpha$ Ni(OH) <sub>2</sub> -NaAl(OH) <sub>4</sub>	28.3

The success of the solution growth process for  $\beta$ -Ni(OH)<sub>2</sub> prompted an investigation of the possibility of forming  $\alpha$ -Ni(OH)<sub>2</sub> by solution growth. Since it was known that substitution of aluminum for nickel ions can influence the formation of  $\alpha$ -Ni(OH)<sub>2</sub>, aluminum ions were introduced into the solution growth bath. The first approach to accomplish this that was investigated was the saturation of the solution growth solution of concentrated aqueous ammonia with both nickel and aluminum hydroxides. The solubility of the latter species is much lower than Ni(OH)<sub>2</sub> and was determined accurately by saturated pure concentrated Ni(OH)<sub>2</sub> with Al(OH)<sub>3</sub>. Three estimates of [Al(OH)<sub>4</sub>]<sup>-</sup> concentration were obtained by using the same approach as that employed for [Ni(NH<sub>3</sub>)<sub>6</sub>]<sup>2+</sup>. The average [Al(OH)<sub>4</sub>]<sup>-</sup> concentration calculated is  $2 \times 10^{-2} \pm 9.22 \times 10^{-4}$  M.

Evaporation of ammonia from the Ni(OH)<sub>2</sub>/Al(OH)<sub>3</sub> solution in concentrated ammonia led to co-precipitation of the metal hydroxides as a single phase, Ni<sub>(1-x)</sub>Al<sub>x</sub>(OH)<sub>(2+x)</sub>. Assuming that all the nickel and aluminum ions are incorporated into the precipitate, x can be calculated from the relative solubilities of the metals. This gives a formula of Ni<sub>0.87</sub>Al<sub>0.13</sub>(OH)<sub>2.13</sub> for the precipitate. The X-ray pattern of this material (Figure 10 (a)) demonstrates that the aluminum content is sufficiently high for formation of the  $\alpha$ -Ni(OH)<sub>2</sub> structure. The XRD reflections are broad and asymmetrical indicating the disordered nature of the stacking sequences of the material. The particle size calculated from the scanning electron micrograph ranges from 0.20 to 1.7  $\mu$ m, the largest particles visibly consist of aggregates of smaller spherical particles (not shown). Alpha Ni(OH)<sub>2</sub> can be indexed on a hexagonal cell Error! Reference source not found. whose lattice parameters can be computed using the following formula:

$$\frac{1}{d_{hkl}^2} = \frac{1}{a^2} (h^2 + hk + l^2) + \frac{l^2}{c^2}$$

h, k, l are the Miller indices which define a crystallographic plane in three dimensions. The reflections at  $2\theta=11.6$  ( $d_{003}=7.63\text{\AA}$ ) and  $35.1$  ( $d_{102}=2.55\text{\AA}$ ) were used to determine the cell parameters c and a:  $a=3.5\text{\AA}$ ,  $c=22.9\text{\AA}$ . The infrared spectrum of Ni<sub>0.87</sub>Al<sub>0.13</sub>(OH)<sub>2.13</sub> shown in Figure 11 shows the characteristic broad  $\nu_{\text{OH}}$  absorption band at  $3483\text{ cm}^{-1}$  for the hydrogen-bonded hydroxyl group of  $\alpha$ -Ni(OH)<sub>2</sub>.

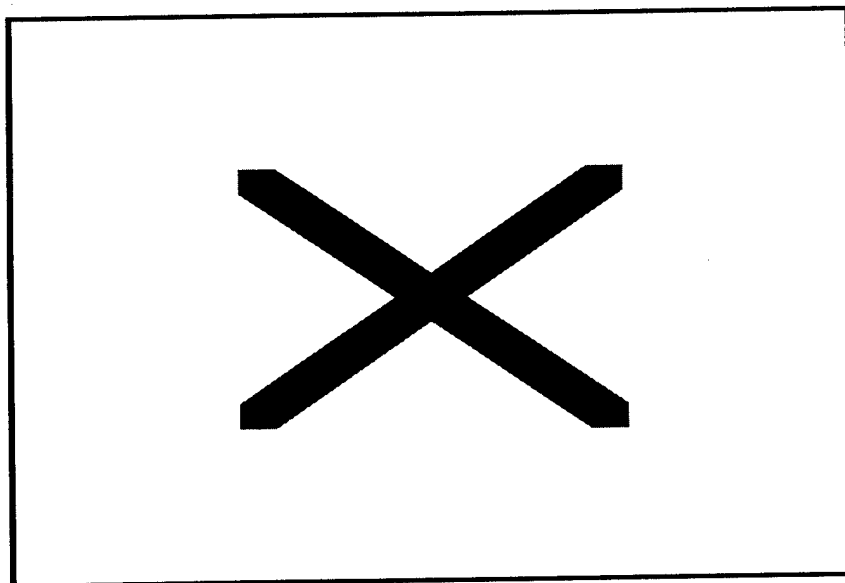


Figure 10. XRD of  $\text{Ni}_{(1-x)}\text{Al}_x(\text{OH})_{(2+x)}$  (a), and  $\text{Ni}(\text{OH})_2\text{-NaAl}(\text{OH})_4$  (b)

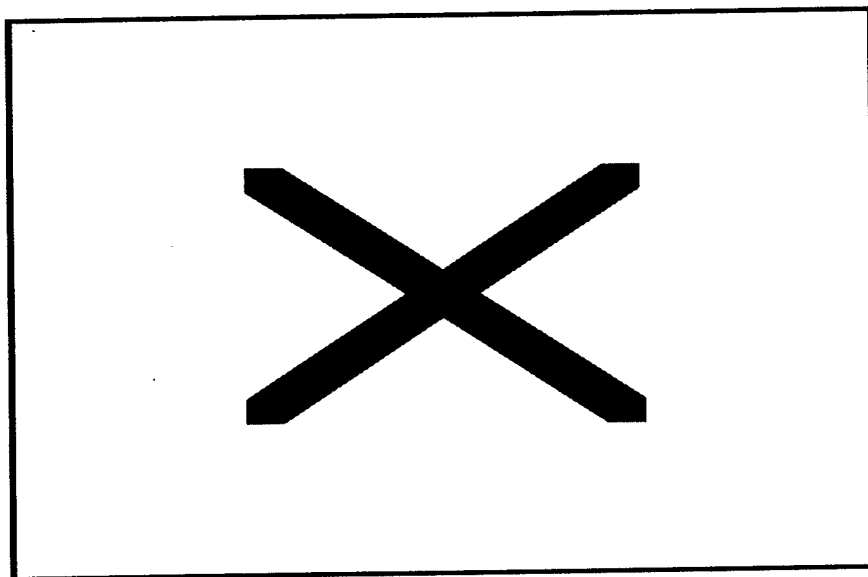


Figure 11. Infrared Spectrum of  $\text{Ni}_{(1-x)}\text{Al}_x(\text{OH})_{(2+x)}$

Doping of  $\text{Ni}(\text{OH})_2$  with aluminum was also achieved by simply introducing sodium aluminate into the solution growth bath. The advantage of this approach resides in the fact that it provides better control of aluminum concentration than saturation of ammonia solution with aluminum hydroxide. Thus it is possible to readily determine the  $\text{Ni(II)/Al(III)}$  ratio required for formation of  $\alpha\text{-Ni}(\text{OH})_2$ . However, it was necessary to collect the green precipitate before

complete evaporation of the solvent to prevent crystallization of excess sodium aluminate onto the nickel hydroxide precipitate.

The various X-ray patterns of  $\text{Ni}(\text{OH})_2$  from the growth solution containing  $\text{NaAl}(\text{OH})_4$  (0.33M) are shown in Figure 12. The addition of 1 ml of  $\text{NaAl}(\text{OH})_4$  (0.33M) (see Fig. 12. (b)) was sufficient to precipitate some  $\alpha$ - $\text{Ni}(\text{OH})_2$  along with the predominantly-formed  $\beta$  phase. The formation of  $\alpha$ - $\text{Ni}(\text{OH})_2$  is progressively favored as the volume of  $\text{NaAl}(\text{OH})_4$  introduced increases (see Fig. 12 (c) and (d)). A pure crystalline alpha form is precipitated from a solution containing 6 ml of  $\text{NaAl}(\text{OH})_4$  and 40 mL of  $\text{Ni}(\text{OH})_2$ -conc. aqueous ammonia solution, as illustrated by Figure 12. (e). The transmission electron micrograph shown in Figure 13 reveals the presence of large ( $0.45\mu\text{m}$ ) spherical  $\text{Ni}(\text{OH})_2$  particles along with blocks of materials composed of sheets that are delaminated at the edges. The  $[\text{Ni}^{2+}]:[\text{Al}^{3+}]$  ratio for formation of the pure alpha-phase was 1:0.35, which is significantly higher than the 1:0.15 ratio of  $\text{Ni}_{0.87}\text{Al}_{0.17}(\text{OH})_{2.13}$  prepared from  $\text{Al}(\text{OH})_3$ . The lattice parameters of the precipitated layered double hydroxide c and a were determined using the 003 and 110 reflections ( $a=2d_{110}$ ) values:  $a=3.5 \text{ \AA}$ ;  $c=23.2 \text{ \AA}$ . The a parameter is higher than the typical 3.0 to 3.1  $\text{\AA}$  reported in the literature. Since Al(III) is smaller than Ni(II), this indicates the content of Al(III) necessary to stabilize the alpha structure by the solution growth method is smaller than that required by the nitrate solution precipitation method. In the latter method, the LDH is obtained at a ratio of Ni:Al of 6.69:1. In the 2.6-3.2  $\text{\AA}$  region, a broad asymmetrical band, typical of turbostratic structures is seen. These X-ray reflections indicate the disordered nature of the  $\text{NiO}_2$  slabs stacking.

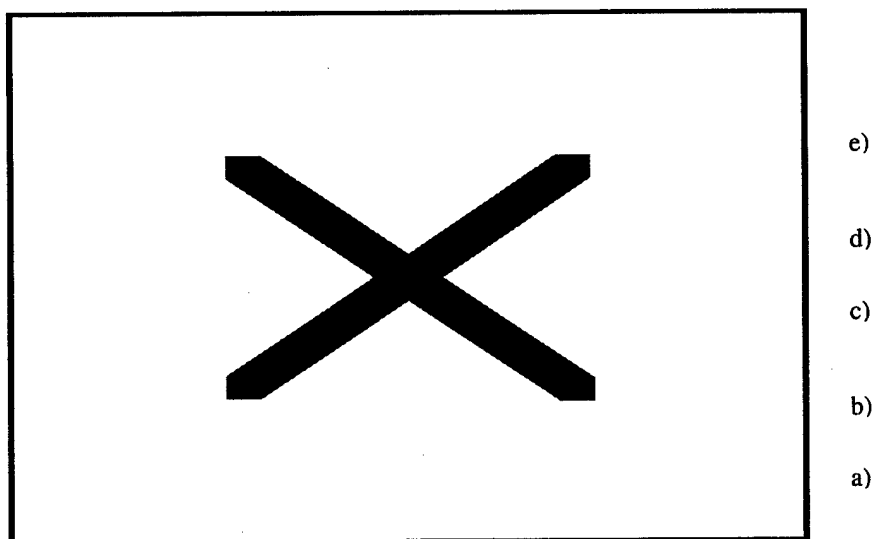


Figure 12. XRD of Solid from 40 mL  $\text{Ni}(\text{OH})_2$ - $\text{NH}_4\text{OH}$  (a), with 1 mL (b), 2 mL (c), 4 mL (d), and 6 mL (e) of  $\text{NaAl}(\text{OH})_4$  (0.33 M) Solution

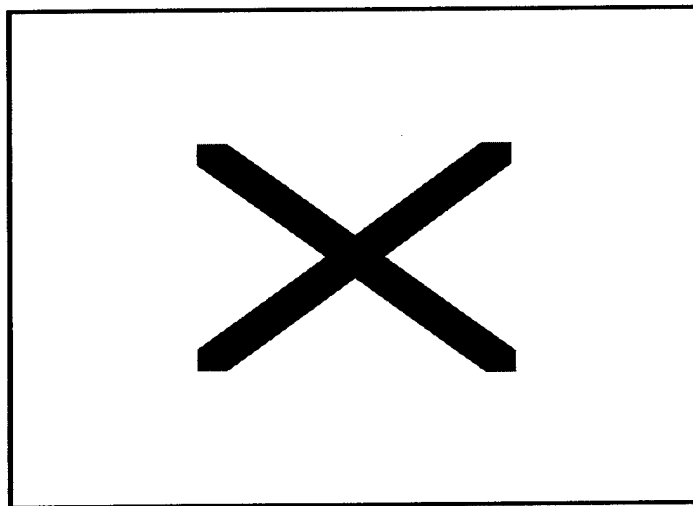


Figure 13. TEM of  $\text{Ni(OH)}_2\text{-NaAl(OH)}_4$  Precipitate

The presence of aluminum ions not only causes the formation of  $\alpha\text{-Ni(OH)}_2$  but it also has a profound effect on the morphology of the product. Unfortunately, the aluminum-containing chemical baths are not amenable to solution growth of  $\alpha\text{-Ni(OH)}_2$  thin films. However this failure is compensated by the ability to form free-standing films at the solution/air interface, along with additional precipitated material at the bottom of the bath. Presumably, the difference from the aluminum-free deposition is a result of substitution of aluminum ions for nickel ions in the  $\text{Ni(OH)}_2$  as it forms. This would produce positively charged particles that would repel each other and resist aggregation into a precipitate on a film. However, as the ammonia rapidly evaporates from solution the particles are carried to the air/solution interface where they aggregate into a film of average thickness 0.10 mm. Possibly, the linking of the particles occurs as the ammonia is lost from nickel ions on the surface of the particles causing particles to link together by formation of hydroxide bridges. Once the original film forms as a skin over the surface of the solution, it continues to grow thicker as more material deposits on its bottom. The net result is an opaque green film that is smooth on the upper surface and rough on the lower side due to random aggregation of particles. The films are somewhat brittle but can be removed from the deposition bath and manipulated carefully by hand. Thus, free-standing films of aluminum-stabilized  $\text{Ni(OH)}_2$  were readily prepared and these could be promising electrode materials.

While in the absence of aluminum, the  $\text{Ni(OH)}_2$ /concentrated ammonia solution mainly deposits thin coatings on the container wall or suspended substrates, it also forms extremely thin, optically transparent skins at the air-water interface. Presumably the thinness is a result of the  $\text{Ni(OH)}_2$  forming films on all available surfaces with a preference for the solid-liquid interface.

Attempts to prepare  $\text{Co(OH)}_2$  films in the same manner as nickel hydroxide failed due to much poorer solubility.

### Exploration of Molybdenum and Tungsten Hydrogen Bronzes for Electrode Materials



In the search for another material with dual proton and electron conductivity several hydrogen bronzes of early d-block metals were examined. It was found that molybdenum blue,  $\text{Mo}_2\text{O}_5(\text{OH})$ , and tungsten blue,  $\text{W}_3\text{O}_8(\text{OH})$ , were electrically-conductive and displayed high hydrogen ion mobility and thus might serve as electrode materials for electrochemical supercapacitors. However, the tungsten compound had the tendency to slowly oxidize in air and may not be suitable for capacitor development. However molybdenum blue did not suffer from this problem. Therefore, a convenient synthesis for  $\text{Mo}_2\text{O}_5(\text{OH})$  via the reaction of molybdenum trioxide with hot alcohols. This study utilized a series of test reactions between  $\text{MoO}_3$  and a variety of alcohols in order to determine the effectiveness of the alcohols for the production of the bronze. The alcohols used in this study were methanol, ethanol, propanol, *isopropanol*, butanol, *isobutanol*, *secbutanol*, *tertbutanol*, 3-methyl-1-butanol, allyl alcohol and benzyl alcohol. The reactions were carried out at  $120^\circ\text{C}$  for 24 h in order to limit the conversion of  $\text{MoO}_3$  to the molybdenum bronze to less than 25%. In this fashion, the rate of the redox reactions were approximated by the initial slopes method. The extent of conversion of  $\text{MoO}_3$  to molybdenum bronze was determined by X-ray powder diffraction using the areas of one X-ray reflection due to  $\text{MoO}_3$  ( $2\theta = 25.10^\circ\text{A}$ ) and one due to molybdenum bronze ( $2\theta = 26.10^\circ\text{A}$ ). The ratio of the areas of the two peaks was used rather than the raw areas to eliminate errors due to sample size or placement in sample holder. Using the linear fit to the calibration curve, the amount of molybdenum bronze in the products obtained from the reaction of  $\text{MoO}_3$  with alcohols could be calculated using and the results are given in Table 3

All of the primary alcohols with the exception of methanol were effective in the synthesis of the bronze with butanol giving the greatest yield of the bronze. The failure of *tert*-butanol to reduce  $\text{MoO}_3$  is not surprising since it contains no  $\alpha$ -hydrogen atoms. Methanol produced a molybdenum oxyformate due to reaction of formaldehyde with the molybdenum bronze. The lack of reaction of *isopropanol* and *sec*-butanol with  $\text{MoO}_3$  indicates considerable steric constraints on the redox reaction. Indeed, *iso*-butanol with a methyl branch on the  $\alpha$ -carbon was also ineffective for the synthesis of molybdenum bronze. Only when the methyl group is introduced into the gamma position ( as in 3-Me-1-butanol) does it not interfere with the bronze production. The ability of alcohols to reduce  $\text{MoO}_3$  likely involves a carbocation mechanism in which a hydride ion is first extracted. In order to gain a better understanding of the hydrogen insertion process, the alcohols (filtrate) obtained on the reaction between  $\text{MoO}_3$  and alcohols were analyzed. Aldehydes were found to be the major products. The results of the analysis are given in Table 4.

Table 3. Percentage of bronze produced from alcohols

Alcohol	Percentage Molybdenum Bronze Produced
Methanol	0
Ethanol	13.6
Propanol	15.7
<i>iso</i> Propanol	0
Butanol	21.7
<i>iso</i> Butanol	3.8
<i>sec</i> Butanol	0
<i>tert</i> Butanol	0
3-Me-1-butanol	13.6
Methoxyethanol	12.8

Allyl Alcohol	14.6
Benzyl alcohol	19.4

Table 4 Analysis of alcohol used in molybdenum bronze synthesis

Alcohol	Major Product	Minor Product
Propanol	Propanaldehyde (95%)	Di- <i>iso</i> -propylether, di- <i>n</i> -propyl ether, <i>isopropyl</i> -propylether (5%)
Butanol	Butyraldehyde (96%)	Sec-butylether, dibutylether, isobutyl-butylether (4%)
Benzylalcohol	Benzaldehyde (95%)	Dibenzyl ether (5%)

The aldehydes are observed as the oxidation products but small amounts of ethers are also observed. It was suspected that the hydrogen bronze catalyzed the conversion of the alcohols to the ethers. This was confirmed by separate experiments between the bronze and alcohols (Table 5).

Table 5. Results of reaction between molybdenum bronze and alcohols

Alcohol	Major Product	Minor Product
Propanol	di- <i>isopropyl</i> ether (95%)	<i>Isopropyl</i> -propyl ether (4%), di-propyl ether (1%)
Butanol	di- <i>secbutyl</i> ether (97%)	di-butyl ether (3%)
Benzyl alcohol	di-benzyl ether (99%)	

Note, that the major ether products from butanol and propanol have undergone a rearrangement of the alkyl groups from primary to secondary moieties. This suggests a carbocation mechanism. Also, the fact that both the alkyl groups are rearranged in the major ether products suggests that the isomerization of alcohols occurs prior to condensation to the ether. Both results indicate a possible Brønsted acid catalyzed mechanism that is shown in Figure 14 for propanol. The preponderance of diisopropyl ether suggests that isomerization of the alcohol occurs more rapidly than ether formation so that the dipropyl ether and propyl isopropyl ether are formed only in small amounts in the early part of the reaction.

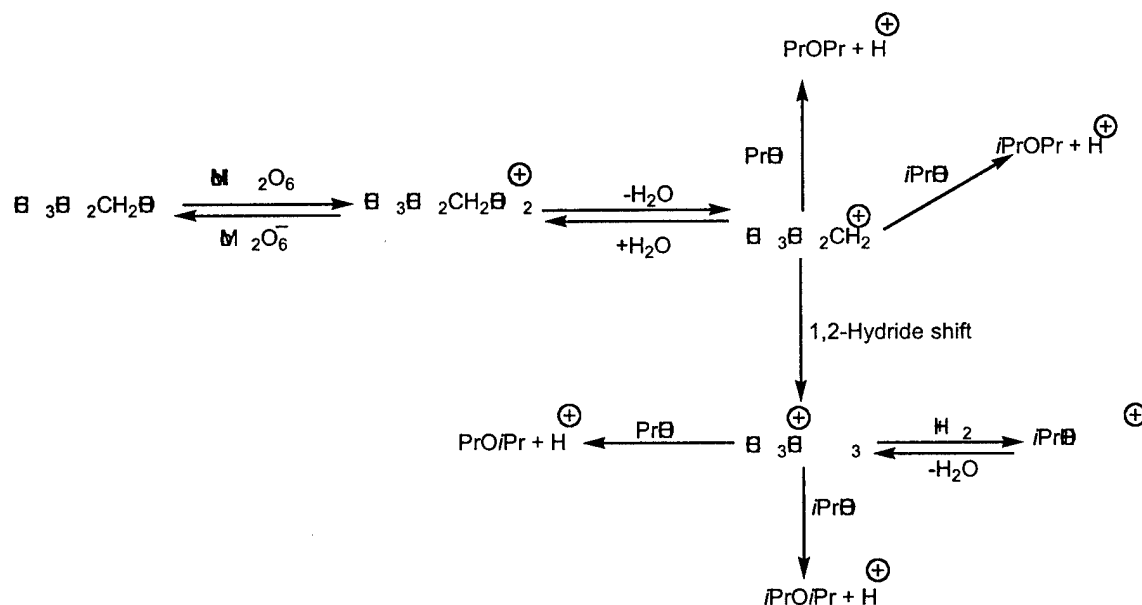


Figure 14: Proposed Mechanism for Reaction of Alcohols with Molybdenum Blue

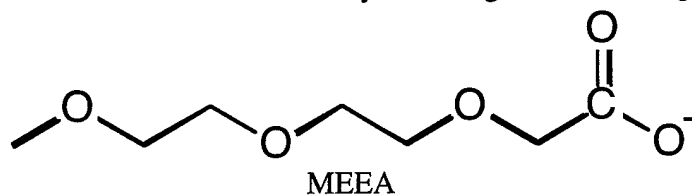
The reduction of molybdenum trioxide with alcohols produced molybdenum hydrogen bronze with limited surface area (22 m<sup>2</sup>/g). Optimization of the surface area was attempted by using a precursor method in which an tetraalkylamine salt of glycolic acid was reacted with molybdenum trioxide in refluxing water to yield (R<sub>4</sub>N)<sub>2</sub>[MoO<sub>2</sub>[glycdian]<sub>2</sub>] where glycdian is the dianion of glycolic acid that is deprotonated at the carboxylate and the alpha-hydroxide (see below for further discussion of the structure). The tetramethyl ammonium and tetrabutylammonium salts were prepared in the hope that the cation can be used to influence the porosity of the MoO<sub>3</sub> and Mo<sub>2</sub>O<sub>5</sub>(OH) derived from it. Unfortunately, these compounds decomposed at 400°C to yield MoO<sub>3</sub> with only a marginal improvement in surface area (ca. 30 m<sup>2</sup>/g). Therefore a method was used that we developed for the synthesis of spherical porous aggregates of nanoparticulate metal oxide. An anion-exchange resin (Dowex 550A) was treated with excess sodium molybdate and the resulting resin was fired at 600°C. This gave porous spherical beads of nanocrystalline MoO<sub>3</sub> but this gradually converted to large crystalline shards of MoO<sub>3</sub> upon standing at room temperature for several days. This instability of extremely high surface area molybdenum oxides made it necessary to abandon the molybdenum hydrogen bronze as an electrode material. However, it might actually be suitable when supported on a conductive high surface area material. For example a hybrid carbon fiber/molybdenum bronze material could be a good electrode. If so, the glycolate-derived MoO<sub>3</sub> precursors would be useful for preparing such a material.

## Single Source Precursors for Bimetallic Oxide Electrode Materials

### Liquid Metal Carboxylate Precursors

The discovery by the Apblett research group of a family of metal carboxylates that are liquids at room temperature has provided novel approaches for the synthesis of ceramic films by liquid phase processing. These air and water-stable carboxylates, are salts of 2-[2-(2-

methoxy)ethoxy]-ethoxyacetate, (MEEA)<sub>2</sub>. It is believed that the polyether linkages contribute to their unusual characteristics of these metal salts by chelating and "solvating" the metal ions.



The utility of these liquid metal carboxylates is markedly enhanced by the fact that they are excellent solvents for other metal salts so that precursor solutions for multi-metallic ceramic materials are readily prepared. For example, a homogeneous precursor solution for nickel ferrite was synthesized by dissolution of  $\text{Ni}(\text{NO}_3)_2$  in the liquid iron carboxylate,  $\text{Fe}_3\text{O}(\text{MEEA})_7 \cdot 5.5(\text{H}_2\text{O})$ . This precursor solution yielded a metastable, amorphous  $\text{NiFe}_2\text{O}_4$  phase at  $300^\circ\text{C}$  demonstrating that these precursors are also useful for generating metastable phases. In this case, the amorphous oxide underwent an exothermic crystallization at  $374^\circ\text{C}$  to yield the trevorite phase of  $\text{NiFe}_2\text{O}_4$ . Similarly, barium titanate has also been synthesized using a liquid metal carboxylate precursor that was prepared by dissolving barium acetate in  $\text{Ti}(\text{MEEA})_4$  and spinel and yttrium aluminum garnet were synthesized at  $800^\circ\text{C}$  from liquid precursors derived from dissolution of magnesium or yttrium nitrate in  $\text{Al}(\text{MEEA})_2\text{OH}$ .

For the purpose of synthesis of strontium ruthenate there are three possible approaches for the preparation of a suitable MEEA-based precursor. Either  $\text{Sr}(\text{MEEA})_2$  or  $\text{Ru}(\text{MEEA})_3$  could be used individually (with addition of appropriate salts of the other metal) or both MEEA salts might be combined. The latter approach is the least economically-favorable due to the expense of the organic acid and the need to synthesize both metal carboxylates. Therefore, this investigation focussed on using a single strontium or ruthenium MEEA salt plus a relatively-inexpensive source of the second metal.

The first task was to prepare the individual MEEA salts.  $\text{Sr}(\text{MEEA})_2(\text{H}_2\text{O})$  was synthesized by refluxing an aqueous solution of strontium hydroxide with two molar equivalents of HMEEA for 12 hours. The resulting pale yellow solution was filtered through a fine glass frit and was evaporated to dryness on a rotary evaporator. After a final drying under high vacuum for 24 hours, a very pale yellow glassy solid was obtained in quantitative yield. Thus,  $\text{Sr}(\text{MEEA})_2(\text{H}_2\text{O})$ , unlike other MEEA complexes, is a solid, a result that is likely due to the typically high coordination number of strontium. However, the solid was amorphous to X-rays, indicating a highly disordered structure glass-like structure conducive to doping with other metal ions. The corresponding ruthenium MEEA complex was prepared by refluxing a mixture of  $\text{Ru}_3\text{O}(\text{acetate})_7(\text{H}_2\text{O})_3$  with nine molar equivalents of HMEEA in toluene. The reaction was driven to completion by collection of the water and acetic acid by-products from the toluene condensate using a Dean-Stark apparatus half-filled with sodium hydroxide. After 48 hours, the solution was filtered through a fine glass frit. Evaporation of the toluene and drying under high vacuum yielded a viscous green liquid which analyzed as  $\text{Ru}(\text{MEEA})_3$ . The yield ranged from 95-98%. This compound is unusual in that it is the first homoleptic ruthenium carboxylate synthesized - most ruthenium carboxylates are basic carboxylates with three ruthenium centers attached to a central oxygen atom. Infrared spectra of the MEEA complex demonstrated that the carboxylates were not bridging between ruthenium centers and cryoscopy in benzene indicated a monomeric structure. The lack of clustering of ruthenium provides a definite advantage for preparation of precursors for strontium ruthenate.

Next, the MEEA salts were mixed with a precursor compound for the other required oxide. In the case of  $\text{Ru}(\text{MEEA})_3$ , strontium nitrate was used. This salt was dissolved in the minimum amount of water and was added to a stoichiometric amount of  $\text{Ru}(\text{MEEA})_3$ . The solvent was removed in vacuo to yield the desired  $\text{SrRuO}_3$  precursor as a dark green, amorphous solid. In similar procedures,  $\text{RuNO}(\text{NO}_3)_3$  and  $\text{Ru}_3\text{O}(\text{acetate})_7(\text{H}_2\text{O})_3$  were dissolved in  $\text{Sr}(\text{MEEA})_2$  to also afford dark green, amorphous solids.

Thermal gravimetric analysis of the  $\text{Sr}(\text{MEEA})_2/\text{Ru}_3\text{O}(\text{acetate})_7(\text{H}_2\text{O})_3$  precursor showed that it decomposed completely to metal oxides at  $900^\circ\text{C}$ . It was discovered that this rather high temperature was due to the formation of a ruthenium metal phase and a strontium carbonate phase during the initial decomposition of the ligand. X-ray powder diffraction (XRD) demonstrated that oxidation of the ruthenium metal to  $\text{RuO}_2$  (which occurs at an appreciable rate above  $800^\circ\text{C}$ ) was followed by reaction with  $\text{SrCO}_3$  to yield  $\text{SrRuO}_3$ . It was found that replacement of ruthenium acetate with ruthenium nitrate prevented the formation of a refractory ruthenium metal phase. The nitrate ions provide an oxidizing atmosphere so that the  $\text{Sr}(\text{MEEA})_2/\text{RuNO}(\text{NO}_3)_3$  precursor decomposes to an oxide phase at  $600^\circ\text{C}$ . The  $\text{Ru}(\text{MEEA})_3/\text{SrNO}_3)_2$  precursor behaved similarly and infrared spectroscopy demonstrated that the two precursors were almost identical. Thus, the metals must exchange ligands when the MEEA and nitrate salts are mixed so that the resulting solid solutions only varied in their nitrate and MEEA content. Since  $\text{RuNO}(\text{NO}_3)_3$  is commercially-available and one of the least expensive ruthenium compounds, it was picked as the best precursors of the two and was developed further.

The thermal gravimetric trace of  $\text{Sr}(\text{MEEA})_2/\text{RuNO}(\text{NO}_3)_3$  is shown in Figure 15. As can be seen, after initial dehydration and pyrolysis of the ligands, there is a plateau in weight loss at  $466^\circ\text{C}$ . The XRD pattern of a powder prepared at this temperature (Figure 16) had X-ray reflections that corresponded to strontium ruthenate ( $\text{SrRuO}_3$ ), strontium carbonate, and ruthenium dioxide.

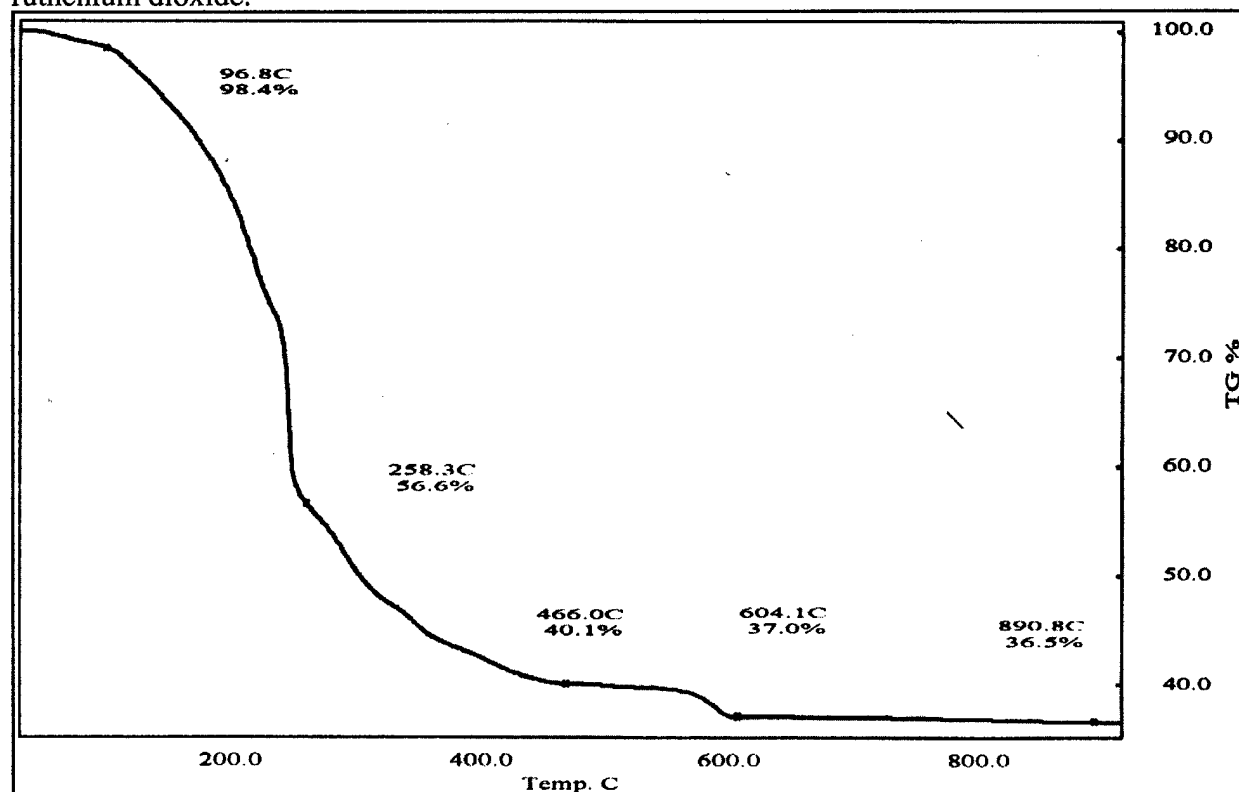


Figure 15. TGA Trace of  $\text{Sr}(\text{MEEA})_2/\text{RuNO}(\text{NO}_3)_3$  Precursor for  $\text{SrRuO}_3$

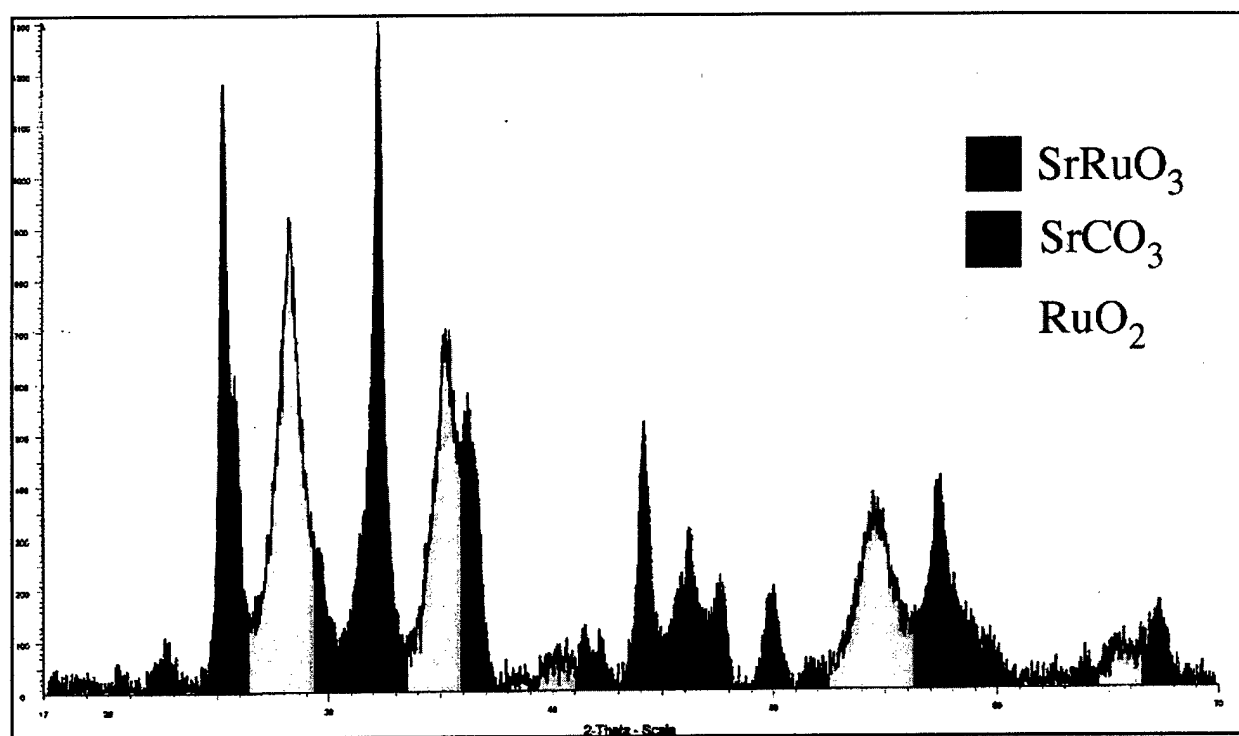


Figure 16. XRD Pattern of Ceramic from Pyrolysis of  $\text{Sr}(\text{MEEA})_2/\text{RuNO}(\text{NO}_3)_3$  at  $470^\circ\text{C}$ .

The strontium carbonate, and ruthenium dioxide phases react with each other in the next weight-loss step that occurs between  $550^\circ\text{C}$  and  $600^\circ\text{C}$ . After this step, the ceramic product is almost pure  $\text{SrRuO}_3$  with a trace of  $\text{RuO}_2$  present (Figure 17). The entire solid still maintains its 1:1 Sr:Ru molar ratio indicating that the  $\text{SrRuO}_3$  phase might be slightly ruthenium deficient. Furthermore, it was found that the small  $\text{RuO}_2$  peaks disappear without a detectable weight loss when the solid is sintered at a temperature of  $1100^\circ\text{C}$ . There is a small weight-loss (0.5%) between  $600^\circ\text{C}$  and  $890^\circ\text{C}$  but infrared spectroscopy demonstrated that it was due to a loss of surface hydroxyls as the strontium ruthenate particles began to grow in size and lessen their surface area.

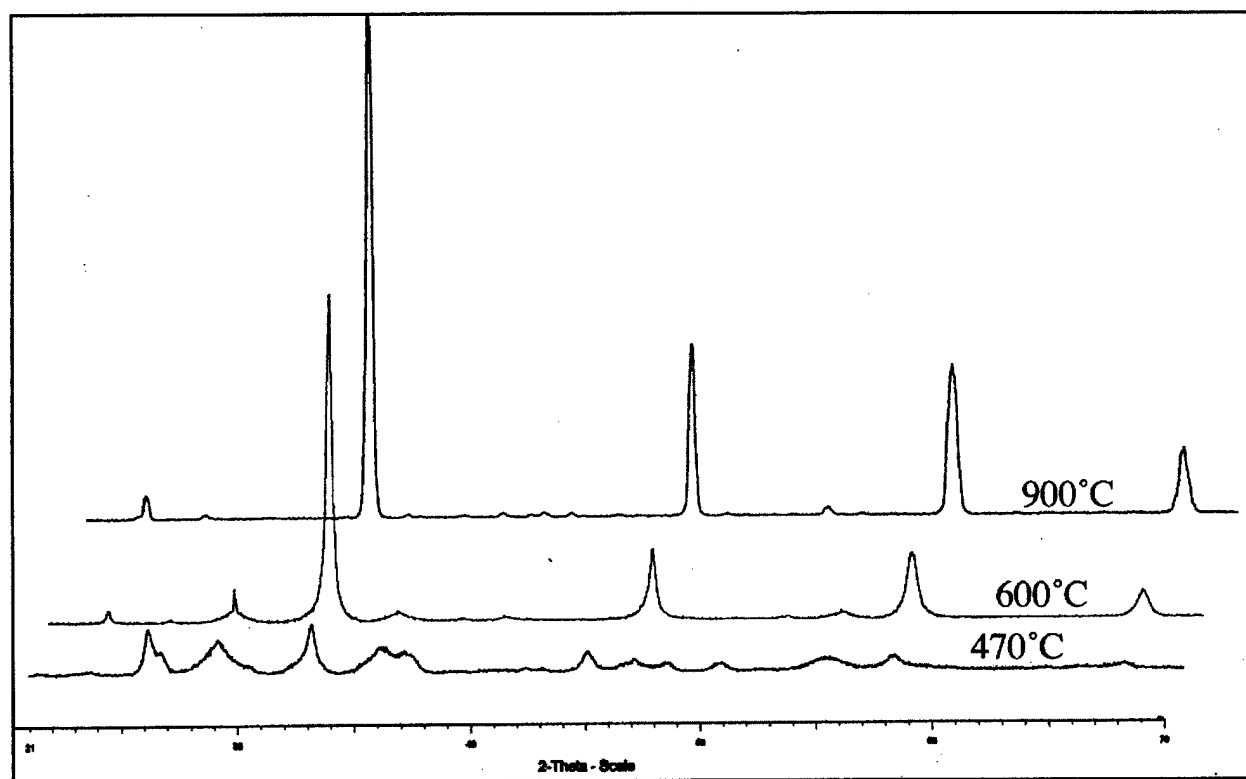


Figure 17. XRD Pattern of Powders from Pyrolysis of  $\text{Sr}(\text{MEEA})_2/\text{RuNO}(\text{NO}_3)_3$

Scherrer analysis of the line widths of the X-ray reflections showed that the  $\text{SrRuO}_3$  initially formed at 470 °C had an average crystallite size of 10.2 nm. At 600 °C, the point at which conversion to  $\text{SrRuO}_3$  is complete, the average crystallite size increases to 20.1 nm. The powder is resistant to sintering and the crystallite size only increases to 22.7 nm at 900 °C and 33.2 nm at 1100 °C. Scanning electron micrographs of the powder obtained at 900 °C (Figure 18) shown that the primary nanometer-sized particles are aggregated into a fibrous sponge-like particles. This porous network forms because the precursor mixture melts before decomposition ensues so that the pyrolysis gases cause the precursor to foam as the solid is deposited. The expansion of the precursor is such that 20 g of precursor will completely fill a 2 liter Erlenmeyer flask with the  $\text{SrRuO}_3$  product.

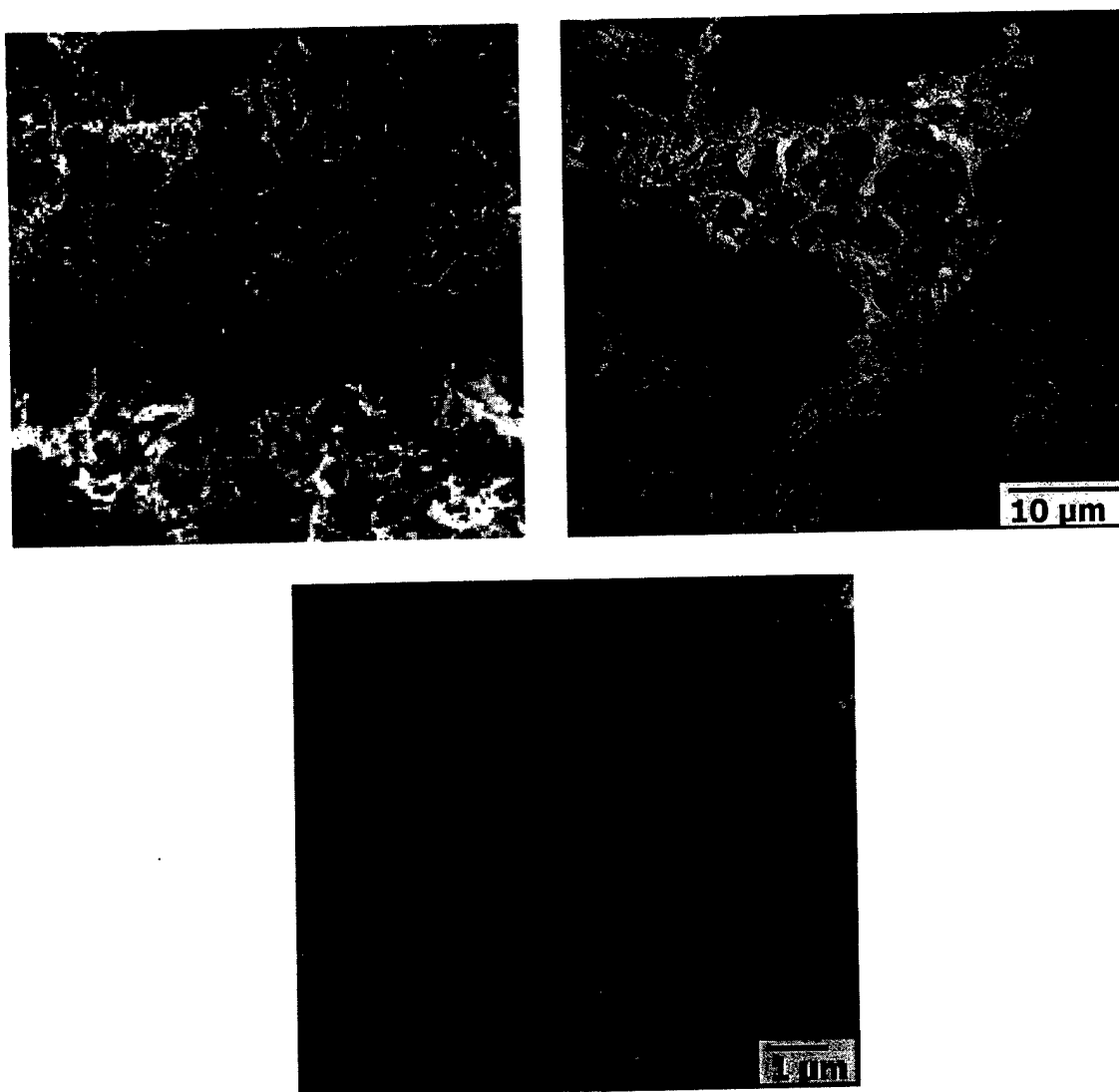


Figure 18. Scanning Electron Micrographs of  $\text{SrRuO}_3$  from  $\text{Sr}(\text{MEEA})_2/\text{RuNO}(\text{NO}_3)_3$  at  $900^\circ\text{C}$

A second type of bimetallic precursor was prepared that combined ruthenium and cobalt in the same compound. Since both cobalt oxides and ruthenium oxides are useful electrode materials for supercapacitors, it can be expected that the mixed oxides might show some advantages.  $\text{Ru}_2\text{CoO}(\text{O}_2\text{CCH}_3)_6$  was prepared according to a literature method and its thermal decomposition was characterized by TGA. It was found to produce an amorphous material at  $225^\circ\text{C}$  that contained a considerable amount of Ru(III). After heating above  $500^\circ\text{C}$ , the ruthenium was oxidized to Ru(IV) and the ceramic phase-separated into  $\text{Co}_3\text{O}_4$  and  $\text{RuO}_2$  (which were clearly detectable as a nanocomposite mixture at  $850^\circ\text{C}$ ). This result is interesting in several ways: the amorphous material has high surface area and may be useful for supercapacitor application while the phase separation process would be expected to produce ruthenium oxide on the outside surface (since it has the lower surface energy) - this might be a way of fabricating high surface-area ruthenium electrodes without using large amounts of ruthenium.

In our investigation of bimetallic precursors based on similar chemistry as that described above for  $\text{MoO}_3$ , we have found that molybdate precursors can be prepared with almost



any metal and any alpha-hydroxy acid. The research focussed on gluconates for high water solubility, glycolates for high ceramic yield, and benzilates for high porosity. The latter carboxylate takes advantage of what was learned concerning high surface area from precursor methods: it has two phenyl groups attached to the alpha-carbon. We have been able to make several benzilate precursors for a variety of molybdates and are trying to optimize conductivity by varying the metal involved. Along the way, we have determined the crystal structure of the potassium salt that proves our conjecture concerning the structure of these precursors (Figure 5). The potassium salt reacts with divalent and trivalent metals to rapidly precipitate the mixed metal molybdate precursor. We have also found that similar chemistry is possible to produce vanadate precursors when an amino acid is used in place of the hydroxyacid and vanadium pentoxide in place of  $\text{MoO}_3$ . This is an exciting result because it makes the full range of amino acids available for designing vanadate precursors.  $\text{V}_2\text{O}_5$  also reacts with hydroxyacids so there is a method for making mixed vanadium/molybdenum oxides in which we can maximize the electrical conductivity,

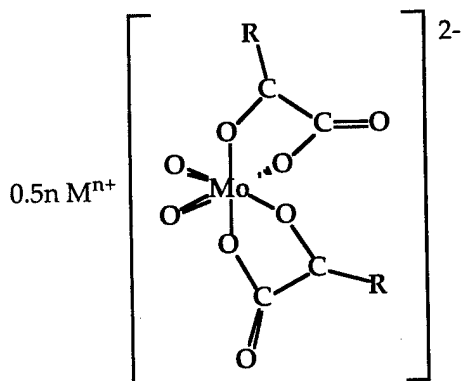


Figure 19. Molybdate Precursor Based on Alpha-Hydroxyacids

The gluconate precursors were used in a search for new, improved electrode materials for supercapacitors. Transition metal gluconates (Mn, Fe, Co, Ni, Cr) were synthesized by reaction of gluconic acid with the corresponding metal hydroxides or carbonates in refluxing water. The salts were isolated by precipitation with methanol and thermal gravimetry was used to determine the degree of hydration. These salts were then heated at reflux in water with molybdenum trioxide (1:1 mole ratio) or vanadium pentoxide (1:2 ratio). Typically the metal oxides reacted and dissolved within a few hours. The mixed metal gluconate dianion salts were then precipitated from aqueous solution by precipitation with methanol. Using these to determine the degree of hydration. These salts were then heated at reflux in water with molybdenum trioxide (1:1 mole ratio) or vanadium pentoxide (1:2 ratio). Typically the metal oxides reacted and dissolved within a few hours. The metal gluconate dianion salts were then precipitated from aqueous solution by precipitation with methanol. The precursors could be converted to metal vanadates and molybdates by heating to 400-600°C. They were used to do a combinatorial study to find candidates for electrode materials for supercapacitors. The desired product was a material that was electrically conductive and had a transition metal with variable oxidation state. The best materials that were found were cobalt vanadates that are bronze metallically-conductive compounds. These are currently being developed into electrochemical supercapacitors. It was also discovered that the vanadate precursors were effective corrosion inhibitors.

The attempts to prepare ruthenate precursors via the gluconate process failed since ruthenium dioxide failed to react with transition metal gluconates even after prolonged heating. However it was found that ruthenium trichloride reacted with molybdenum trioxide to yield an amorphous electrically-conductive compound. The synthesis of this material is being optimized and it will then be incorporated into electrochemical supercapacitors. It was found that such reactions of  $\text{MoO}_3$  were possible for a wide range of heavier transition, lanthanide, actinide, and main group metals. It is very selective for these and not for light metals. This technology has therefore been spun off into processes for heavy metal remediation.

We have also used an alternative precursor route to produce nanocrystalline solids that could be useful for electrode applications. These precursors are based on pyruvic acid oxime, an anion that decomposed by the concerted decomposition to produce acetonitrile, water, and carbon dioxide as gaseous by-products (Figure 6). Since this reaction occurs at low temperature and the gases evolve rapidly, the result is a high surface area metal oxide. In the case of ruthenium, however,  $\text{Ru}_3\text{O}(\text{PAO})_7$  was found to produce nanocrystalline (ca. 3 nm) ruthenium metal. Analysis of the by-products demonstrated a radical mechanism that yielded dimethylglyoxime as a radical coupling product. The ability to produce such fine ruthenium metal at low temperature without a reducing agent is likely to have important applications in catalysis. The PAO precursor method was used to prepare  $\text{CuCo}_2\text{O}_4$  as a nanocrystalline solid at  $250^\circ\text{C}$ . This is a promising anode material for alkaline water electrolysis. The precursors are simply prepared by co-precipitating  $\text{Co(II)}$  and  $\text{Cu(II)}$  from aqueous solution to yield a solid solution of the PAO complexes.

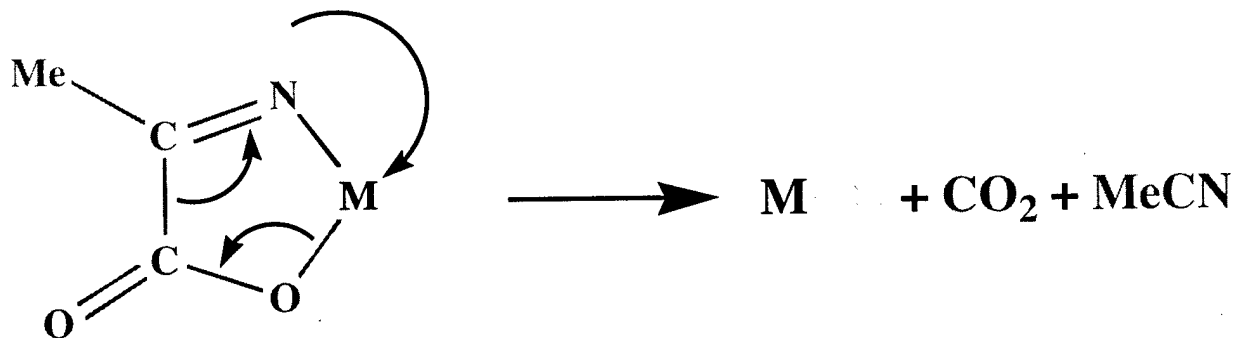


Figure 6. Decomposition of PAO Complexes

## REFERENCES

- [1] H. Schafer, G. Schneidereit, W. Gerhardt, *Z. Anorg. Allg. Chem.* **1963**, 319, 372.
- [2] B. Cornell, D. J. Simonsson, *Electrochem. Soc.* **1993**, 140, 3123.
- [3] A. Cimino, S. Carra, in *Electrodes of Conductive Metallic Oxides-Part A* (Ed.: S. Trasatti), Elsevier, New York, **1980**, p. 97.
- [4] B. E. Conway, *Electrochemical Supercapacitors, Scientific Fundamentals and Technological Applications*, Kluwer Academic/Plenum Publishers, New York, **1999**.
- [5] D. R. Rolison, P. L. Hagans, K. E. Swider, J. W. Long, *Langmuir* **1999**, 15, 774.

- [6] J. P. Zheng, C. P.J., T. R. Jow, *Hydrous Ruthenium Oxide as an Electrode Material for Electrochemical Capacitors*, *J. Electrochem. Soc.* **1995**, 142, 2699.
- [7] J. W. Long, K. E. Swider, C. I. Merzbacher, D. R. Rolison, *Voltammetric Characterization of Ruthenium Oxide-Based Aerogels and Other RuO<sub>2</sub> Solids: The Nature of Capacitance in Nanostructured Materials*, *Langmuir* **1999**, 15, 780.
- [8] S. Trasatti, *Electrochim. Acta.* **1991**, 36, 225.
- [9] S. Hadzi-Jordanov, M. Vukovic, H. A. Kozłowska, B. E. Conway, *Reversibility and Growth Behaviour of Surface Oxide Films of Ruthenium Electrodes*, *J. Electrochem. Soc.* **1978**, 125, 1471.
- [10] R. W. Vest, (Ed.: R. A. Haber), Noyes Publications, Park Ridge, N.J., **1992**, pp. 303.
- [11] J. V. Mantese, A. L. Micheli, A. H. Hamdi, R. W. Vest, *Metal Organic Deposition*, *M.R.S. Bull.* **1989**, XIV, 1173.
- [12] P. Legzdins, R. W. Mitchell, G. L. Rempel, J. D. Ruddick, G. Wilkinson, *J. Chem. Soc. (A)* **1970**, 3322.